Impact of Redundant Actuation on a 3-DOF Tensegrity Mechanism

Karol Muñoz, Mathieu Porez, and Philippe Wenger

Abstract This paper investigates the impact of redundant actuation on the operational capabilities of 3-DOF tensegrity mechanisms derived from a tensegrity prism architecture. Two mechanisms are considered. The first corresponds to a three-cable tensegrity prism mechanism previously proposed in earlier work., while the second is an improved variant that introduces an additional central actuation cable connecting the fixed and moving platforms, enabling co-actuation. The influence of this actuation redundancy on the geometric workspace (GW) and the wrench feasible workspace (WFW) is analyzed. The three-cable mechanism exhibits limited and asymmetric behavior, resulting in a non-uniform feasible wrench (FW) domain. In contrast, the four-cable mechanism regularizes the kinematic behavior and yields a more isotropic FW, significantly enhancing the operational capabilities of the mechanism and making it more suitable for modular robotic applications.

1 Introduction

Tensegrity mechanisms have attracted increasing interest in robotics due to their lightweight architecture, inherent compliance, and ability to redistribute internal forces through cable actuation [1, 2]. By combining compression and tension elements, these mechanisms exhibit a favorable strength-to-weight ratio and an intrinsic

K. Muñoz
Nantes Université, École Centrale Nantes, LS2N, UMR 6004, F-44000, Nantes, France
e-mail: karol.munoz-salas@ls2n.fr

M. Porez
IMT Atlantique, LS2N, UMR 6004, F-44000 Nantes, France
e-mail: mathieu.porez@imt-atlantique.fr

P. Wenger
Nantes Université, École Centrale Nantes, CNRS, LS2N, UMR 6004, F-44000 Nantes, France
e-mail: philippe.wenger@ls2n.fr

capacity to adapt their stiffness to task requirements, which are desirable properties for robotic systems operating in human-centered environments [3, 4].

These characteristics make tensegrity-based architectures particularly suitable for collaborative and human-centered robotics, where safety, adaptability, and robustness under external interactions are key requirements [2, 5]. As a result, tensegrity mechanisms have been investigated as compliant robotic joints, deployable structures, and modular building blocks for parallel manipulators and reconfigurable robots [6–9].

Within this context of modular and compliant robotic joints, a 3-DOF tensegrity mechanism actuated by three cables was introduced and analyzed in [10]. That work investigated its kinematic behavior and static equilibrium, showing that the geometric workspace (GW) is mainly governed by bar collisions. However, it also revealed intrinsic limitations of the three-cable architecture, including a potential loss of integrity under certain operating conditions. To overcome these limitations, a redundant actuation strategy based on the introduction of a central cable connecting the fixed and moving platforms was proposed. This additional cable is commanded independently and primarily used to regulate the internal force distribution, thereby enforcing a desired torsional state and preserving the integrity condition throughout the operational workspace. Despite this advancement, a quantitative assessment of how actuation redundancy, and in particular the introduction of a fourth cable, impacts the global operational capabilities of the mechanism remains missing.

This paper builds upon the analysis presented in [10] by conducting a comparative study of two 3-DOF tensegrity mechanisms actuated with three and four cables, hereafter referred to as the three-cable mechanism and the four-cable mechanism, respectively. The GW and the wrench feasible workspace (WFW) are analyzed within a unified framework, highlighting the impact of redundant actuation on the operational capabilities of the mechanism.

The remainder of this paper is organized as follows. Section 2 introduces the architecture of the considered tensegrity mechanisms. Section 3 analyzes the geometric workspace. Section 4 presents the wrench-feasible workspace analysis. Finally, Section 5 concludes the paper and outlines future work.

2 Description of the mechanisms

The mechanism consists of a fixed lower platform, a moving upper platform, and three bars connected by spherical joints, forming a prismatic tensegrity mechanism inspired by the tensegrity prism originally described by Burkhardt [11], as illustrated in Fig. 1. Peripheral cables connect alternate vertices of the two platforms, with symmetric anchoring points that coincide with the bar attachment locations in the configuration considered in this work. The orientation of the moving platform is described using the tilttorsion parametrization introduced in [12]. In this representation, the angles ϕ and θ define the tilt of the moving platform, while the angle σ describes its torsional rotation about the central axis, as shown in Fig. 1(a). In

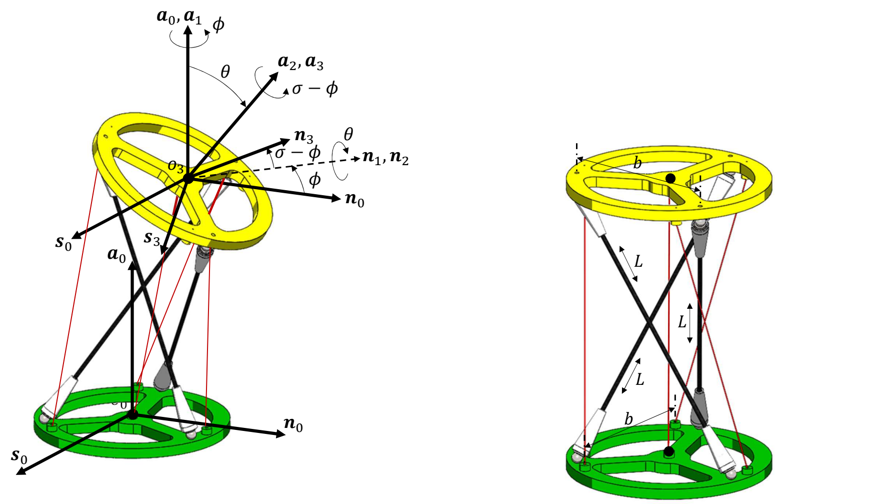

(a) Tilt and torsion parametrization and reference frames.

(b) Geometric parameters and design variables.

Fig. 1: Architecture of the 3-DOF tensegrity mechanism.

conventional terminology, θ corresponds to a pitch rotation, ϕ to a roll rotation, and σ to a yaw rotation about the central axis.

Two actuation schemes are investigated, corresponding to the three-cable mechanism and the four-cable mechanism. The three-cable mechanism employs only the three peripheral crossed cables, resulting in a minimally actuated configuration of the considered 3-DOF tensegrity architecture. The four-cable mechanism retains the same geometric layout and introduces an additional central cable, aligned with the main axis of the mechanism, which connects the centers of the fixed and moving platforms and provides a redundant actuation scheme. Both configurations were presented in [10]. For the analyses presented in this work, the mechanism geometry is parameterized by the ratio L/b, where L denotes the bar length and b the side length of the equilateral platforms defining the triangular arrangement of the bar anchoring points, as shown in Fig. 1(b). This ratio characterizes the slenderness of the mechanism and is used as a key design parameter in the following sections.

3 Geometric Workspace Analysis

The GW and the detection of bar collisions are evaluated using the inverse kinematic model, following the approach introduced in [13]. In the collision analysis, each bar is modeled as a cylinder with a diameter of 5 mm. To characterize the geometric limitations imposed by bar–bar collisions, a parametric study is conducted over the orientation domain $\{\theta, \phi, \sigma\}$ for different values of the slenderness ratio

L/b. For each pair $(\sigma, L/b)$, collisions are evaluated over the full azimuthal range $\phi \in [0°, 360°]$, and the admissible pitch motion is characterized by the scalar GW measure ρ_g, expressed in degrees. The quantity ρ_g represents the size of the largest continuous pitch workspace around the reference configuration $\theta = 0$ that remains collision-free for all ϕ. Since the mechanism exhibits a threefold rotational symmetry about its central axis, the azimuthal angle ϕ does not affect the collision conditions. Consequently, the GW results can be represented in the reduced parameter space $(\sigma, L/b)$.

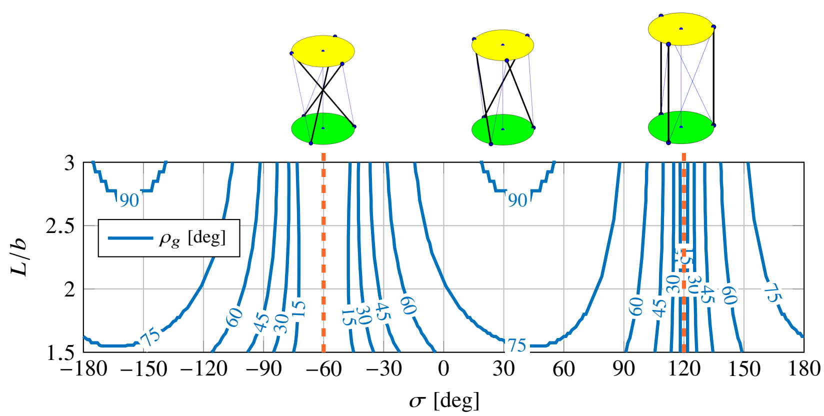

Fig. 2: Influence of the torsional angle σ and the slenderness ratio L/b on the collision-limited geometric workspace measure ρ_g.

Figure 2 reports the resulting collision-limited geometric workspace measure ρ_g as a function of the torsional angle σ and the slenderness ratio L/b, obtained by evaluating collisions over the full azimuthal range $\phi \in [0°, 360°]$. The results show that ρ_g strongly depends on the torsional orientation. Two characteristic configurations define the workspace boundaries: a crossed-bar configuration occurring at $\sigma = -60°$ and a parallel-bar configuration at $\sigma = 120°$. At these configurations, ρ_g vanishes for all considered slenderness ratios, thereby delimiting a common admissible torsional interval $-60° \leq \sigma \leq 120°$. For intermediate values of σ, ρ_g increases with the slenderness ratio, since larger values of L/b delay the onset of bar collisions and allow wider tilt motions. Since both the three-cable and four-cable mechanisms share the same bar geometry and bar connectivity, the resulting GW is identical for both architectures. The geometry-dependent orientation limits identified here are subsequently adopted as a common reference domain for the WFW analysis.

4 Wrench Feasible Workspace Analysis

This section addresses the wrench capabilities of the mechanism based on a static analysis using the kinematicstatic dual formulation introduced by Merlet [14].

In this work, the wrench capabilities are evaluated over a discretized set of platform orientations. Although this approach does not compute the complete wrench-feasible workspace in a strict mathematical sense, it provides a configuration-based approximation of the admissible wrench capabilities of the mechanism. For simplicity, this quantity is referred to as the WFW in the remainder of the paper.

For a cable-driven parallel mechanism, the differential kinematic relationship can be written as

$$\mathbf{A}_A\,\mathbf{S}_0 + \mathbf{A}_P \begin{bmatrix} \mathbf{V}_0 \\ \dot{\boldsymbol{\Omega}}_0 \end{bmatrix} = \mathbf{0}, \tag{1}$$

where $\mathbf{S}_0$ contains the cable length rates, $\mathbf{V}_0$ and $\dot{\boldsymbol{\Omega}}_0$ denote the linear and angular velocities of the moving platform, and $\mathbf{A}_A$ and $\mathbf{A}_P$ are the actuator and platform Jacobian matrices, respectively.

By screw duality, the corresponding static equilibrium relation is expressed as

$$\mathbf{A}^\top \mathbf{f}_c = \mathbf{w}, \qquad \mathbf{A} \equiv \mathbf{A}_A, \tag{2}$$

where $\mathbf{f}_c = [f_{c1}\ f_{c2}\ \ldots\ f_{cN}]^\top$ is the vector of cable tensions and $\mathbf{w} = [\mathbf{F}^\top\ \mathbf{M}^\top]^\top \in \mathbb{R}^6$ denotes the wrench acting on the moving platform. In this static analysis, inertial and gravitational effects are neglected and the platform is assumed to be massless. Each column $\mathbf{a}_i$ of $\mathbf{A}$ represents the unit wrench generated by cable i.

Based on the static equilibrium formulation introduced above, the GW alone is not sufficient to characterize the operational orientations of the mechanism. While the GW defines configurations that are free of bar collisions and kinematic singularities, additional restrictions arise from the static analysis. In particular, actuation singularities occur when one or more cables reach their minimum allowable length, which limits the transmission of static wrenches. Using this framework, a length-limit configuration is identified for the four-cable mechanism at the home configuration, corresponding to $\sigma = -30°$. Although this posture lies within the GW, one or more cables approach their minimum admissible length, causing the effective moment arms of the lateral cables to collapse and preventing the generation of torsional wrenches. For other platform orientations, this limit may occur at larger values of σ. Consequently, $\sigma = -30°$ is adopted as a practical upper bound for the WFW analysis, which is therefore restricted to the interval $-60° \le \sigma \le -30°$.

With the static equilibrium relation established and the admissible orientation domain defined, the Feasible Wrench capabilities of the mechanism can now be characterized. For a fixed posture (ϕ, θ, σ), the set of external wrenches that can be balanced by the cable network under bounded cable tensions is given by

$$\mathcal{W} = \left\{ \mathbf{w} \in \mathbb{R}^6 \;\middle|\; \mathbf{w} = \mathbf{A}^\top \mathbf{f}_c,\ 0 \le f_{\min} \le f_i \le f_{\max},\ i = 1, \ldots, N \right\}, \tag{3}$$

where N denotes the number of cables of the mechanism. The set $\mathcal{W}$ corresponds to a convex polytope, referred to as the FW polytope. Its shape is configuration dependent and reflects both the cable routing and the geometric characteristics encoded in the matrix $\mathbf{A}$.

FW polytopes obtained for four representative configurations, denoted as H, A, B, and C, corresponding to $(\phi, \theta) = (0°, 0°)$, $(0°, 45°)$, $(120°, 45°)$, and $(240°, 45°)$, respectively, are shown in Fig. 3. For all cases, the torsional angle is fixed to $\sigma = -35°$, and the slenderness ratio is set to $L/b = 2$ ($L = 0.18$ m, $b = 0.09$ m).

For each configuration, FW polytopes are shown for both the three-cable and four-cable mechanisms. The orange polytope corresponds to the four-cable mechanism, while the purple polytope represents the three-cable architecture. The largest centered square that can be inscribed in each planar projection is shown in yellow, whereas the projection of the largest centered cube inscribed in the three-dimensional FW polytope is shown in green. All projections are expressed in terms of the normalized wrench components $\Gamma_i/f_{\max}$, which can be interpreted as equivalent lever arms expressed in meters.

For the three-cable mechanism, the FW polytope exhibits a strongly anisotropic structure. While relatively large regions appear in the $\Gamma_x/f_{\max} - \Gamma_y/f_{\max}$ plane, the polytope becomes extremely thin along the torsional direction $\Gamma_z/f_{\max}$ and may pass through the origin. As a consequence, no centered cube can be inscribed and no isotropic wrench index can be defined, indicating that the mechanism cannot generate bidirectional torsional wrenches. In contrast, the four-cable mechanism produces a closed FW polytope around the origin for all tested configurations. The largest centered cube is therefore well defined, and its edge length defines the isotropic wrench index ρ_w. Overall, the additional cable preserves the planar wrench capability while rendering the torsional component Γ_z bidirectional, thereby closing the FW space and improving the robustness of the mechanism under multidirectional loading.

Based on these observations, the WFW analysis is conducted exclusively for the four-cable mechanism. The WFW is characterized by evaluating the configuration-dependent wrench capability over an admissible orientation domain. To this end, the mechanism is numerically evaluated over a discretized set of 64 platform orientations (ϕ, θ) obtained from an 8×8 uniform grid with $\phi \in [0°, 360°]$ and $\theta \in [0°, 90°]$. The torsional angle is restricted to the interval $\sigma \in [-60°, -30°]$, corresponding to the GW-admissible domain further limited by cable length constraints. The resulting distribution of the average WFW measure is shown in Fig. 4.

Figure 4 combines the average WFW measure $\overline{\rho}_w$ with representative contours of the geometric workspace measure ρ_g in the $(\sigma, L/b)$ parameter space. The two ρ_g curves correspond to admissible pitch ranges of 30° and 45°, respectively, and are included for illustration to indicate the collision-limited geometric constraints imposed by bar–bar interactions. Within this admissible domain, the contours of $\overline{\rho}_w$ reveal a strong dependence on the torsional angle σ. For all considered values of the slenderness ratio L/b, the average WFW reaches a maximum in the vicinity of $\sigma \approx -33°$, identifying a torsional configuration that maximizes the average isotropic wrench capability of the mechanism. Importantly, the ρ_g contours show that this

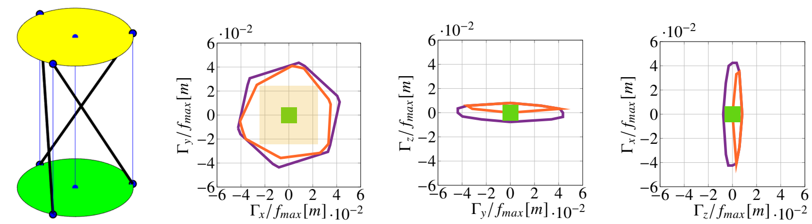

(a) CAD view of the configuration $\boldsymbol{H}$. (b) $\Gamma_x/f_{\max} - \Gamma_y/f_{\max}$ (c) $\Gamma_y/f_{\max} - \Gamma_z/f_{\max}$ (d) $\Gamma_z/f_{\max} - \Gamma_x/f_{\max}$

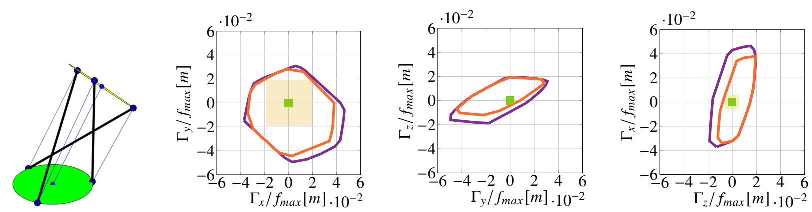

(e) CAD view of the configuration A. (f) $\Gamma_x/f_{\max} - \Gamma_y/f_{\max}$ (g) $\Gamma_y/f_{\max} - \Gamma_z/f_{\max}$ (h) $\Gamma_z/f_{\max} - \Gamma_x/f_{\max}$

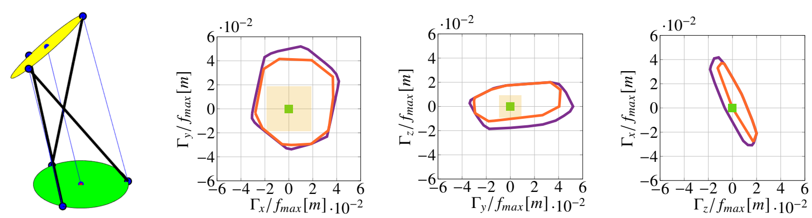

(i) CAD view of the configuration $\boldsymbol{B}$. (j) $\Gamma_x/f_{\max} - \Gamma_y/f_{\max}$ (k) $\Gamma_y/f_{\max} - \Gamma_z/f_{\max}$ (l) $\Gamma_z/f_{\max} - \Gamma_x/f_{\max}$

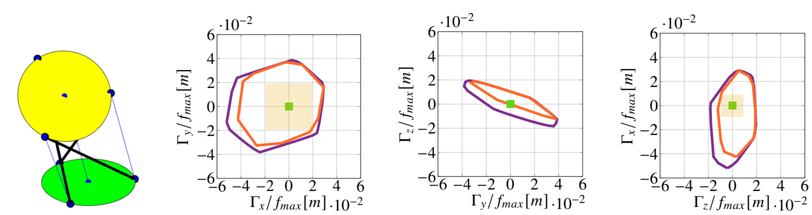

(m) CAD view of the configuration $\boldsymbol{C}$. (n) $\Gamma_x/f_{\max} - \Gamma_y/f_{\max}$ (o) $\Gamma_y/f_{\max} - \Gamma_z/f_{\max}$ (p) $\Gamma_z/f_{\max} - \Gamma_x/f_{\max}$

Fig. 3: CAD views and planar projections of the FW polytopes for configurations H (a–d), A (e–h), B (i–l), and C (m–p).

region of maximum $\overline{\rho}_w$ lies strictly inside the admissible geometric domain and does not coincide with extreme values of ρ_g. This confirms that geometric admissibility is a necessary but not sufficient condition for optimal force transmission: while ρ_g defines the feasible orientation domain, $\overline{\rho}_w$ identifies the torsional configurations that are mechanically optimal within that domain.

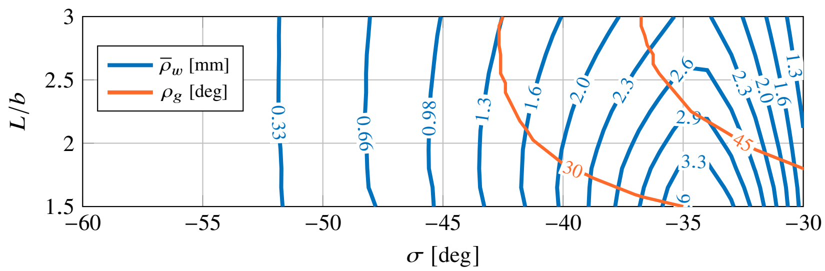

Fig. 4: Influence of the torsional angle σ and the slenderness ratio L/b on the average normalized wrench feasible workspace measure ρ_w.

5 Conclusions and Future Work

This paper presented a comparative static analysis of a 3-DoF tensegrity mechanism actuated with three cables and an improved architecture obtained by introducing a redundant central cable. Although both mechanisms share the same geometric workspace, their static capabilities differ significantly. The three-cable mechanism produces an open feasible wrench domain and cannot generate bidirectional torsional wrenches, whereas the four-cable mechanism yields a closed FW polytope and a non-zero isotropic wrench bound. These results highlight the key role of actuation redundancy in improving the multidirectional wrench capabilities of tensegrity mechanisms.

Future work will extend this analysis toward dynamic modeling and tension-based control strategies. In addition, a laboratory prototype of the four-cable mechanism has been developed, which will serve as an experimental platform for validating the proposed static modeling framework.

References

1. R. E. Skelton and M. C. de Oliveira. *Tensegrity Systems*. Springer, 2009.
2. D. S. Shah, J. W. Booth, R. L. Baines, K. Wang, M. Vespignani, K. E. Bekris, and R. KramerBottiglio. Tensegrity robotics. *Soft robotics*, 2021.

3. M. Arsenault and C. M. Gosselin. Kinematic, static and dynamic analysis of a planar 2-DOF tensegrity mechanism. *Mechanism and Machine Theory*, 41(9):1072–1089, 2006.
4. J. M. Mirats-Tur, J. Camps, J. Hernández, and C. M. Gosselin. Tensegrity frameworks: Static analysis review. *Mechanism and Machine Theory*, 61:1–18, 2013.
5. Yixiang L., Qing B., Xiaoming Y., Jiang W., Bin Y., and Yibin L. A review on tensegrity structures-based robots. *Mechanism and Machine Theory*, 168:104571, 2022.
6. C. Paul and H. Lipson. Design and control of tensegrity robots for locomotion. *IEEE Transactions on Robotics*, 22(5):944–957, 2006.
7. M. Vespignani, J. M. Friesen, V. SunSpiral, and J. Bruce. Design of superball v2. In *IEEE/RSJ International Conference on Intelligent Robots and Systems*, pages 2865–2871, 2018.
8. S. Ikemoto, K. Tsukamoto, and Y. Yoshimitsu. Development of a modular tensegrity robot arm capable of continuous bending. *Frontiers in Robotics and AI*, 8:774253, 2021.
9. J. M. Friesen, J. L. Dean, T. Bewley, and V. SunSpiral. A tensegrity-inspired compliant 3-dof joint. In *IEEE International Conference on Robotics and Automation*, pages 3301–3306, 2018.
10. K. Muñoz, M. Porez, and P. Wenger. Kinematic and static analyses of a 3-dof spatial tensegrity mechanism. In *International Symposium on Advances in Robot Kinematics*, pages 314–323. Springer, 2024.
11. R. W. Burkhardt. *A practical guide to tensegrity design*. Cambridge USA, 2008.
12. I. A. Bonev, D. Zlatanov, and C. M. Gosselin. Advantages of the modified euler angles in the design and control of pkms. In *Parallel Kinematic Machines International Conference*, pages 171–188, 2002.
13. K. Muñoz, M. Porez, and P. Wenger. Modeling and analysis of a four-leg tensegrity mechanism. *Mechanism and Machine Theory*, 211:106009, 2025.
14. J.P. Merlet. Direct kinematics and static analysis of parallel manipulators using a distance matrix. *International Journal of Robotics Research*, 11(4):326–333, 1992.